

# Submillimeter Fourier-transform spectrometer measurements of atmospheric opacity above Mauna Kea

E. Serabyn, E. W. Weisstein, D. C. Lis, and J. R. Pardo

We present accurately calibrated submillimeter atmospheric transmission spectra obtained with a Fourier-transform spectrometer at the Caltech Submillimeter Observatory on Mauna Kea, Hawaii. These measurements cover the 0.9–0.3-mm wavelength range and are the first in a series aimed at defining the terrestrial long-wave atmospheric transmission curve. The 4.1-km altitude of the Mauna Kea site provides access to extremely low zenith water-vapor columns, permitting atmospheric observations at frequencies well above those possible from sea level. We describe the calibration procedures, present our first well-calibrated transmission spectra, and compare our results with those of a single-layer atmospheric transmission model, AT. With an empirical best-fit continuum opacity term included, this simple single-layer model provides a remarkably good fit to the opacity data for H<sub>2</sub>O line profiles described by either van Vleck–Weisskopf or kinetic shapes. © 1998 Optical Society of America  
*OCIS codes:* 010.0010.

## 1. Introduction

Whereas pressure broadening of the H<sub>2</sub>O molecule's many far-infrared (FIR) rotational transitions renders the FIR terrestrial atmosphere opaque, to either side of the FIR the opacity declines<sup>1,2</sup> (with occasional interruption by outlying transitions). This opacity falloff likely reflects the superposition of the far wings of the ensemble of FIR H<sub>2</sub>O rotational transitions, but simple sums over these lines by use of classical collisional line shapes fail to reproduce the magnitude of the absorption far from band center.<sup>2–7</sup> As a result, long-wave (millimeter, submillimeter) opacity models tend to make up the opacity deficit by including an empirical continuum opacity term such as a frequency power law.<sup>3–6</sup> Because distant line wings reflect the intermolecular potential between collision partners, this broadband opacity is of fundamental quantum-mechanical interest, and recent quantum treatments<sup>8–10</sup> show promise in reproducing H<sub>2</sub>O far-wing absorption. Far-wing absorption is also of

great practical importance because it affects astronomy, remote sensing, communications, and atmospheric thermal balance at wavelengths ranging from the radio to the infrared.

The gradual transition between the opaque FIR sky and the transparent radio regime occurs largely at millimeter wavelengths at sea level, but at high mountaintop sites lower levels of H<sub>2</sub>O vapor shift this opacity falloff to the submillimeter band. This wavelength shift permits an important shift in measurement techniques, from narrow-band heterodyne detection<sup>11–13</sup> to broadband spectroscopy. Indeed, early broadband Fourier-transform spectrometer (FTS) measurements of the atmosphere's long-wave opacity falloff exist,<sup>4,14–16</sup> but the data are limited. We have therefore initiated a series of measurements of the terrestrial atmosphere's long-wave opacity spectrum, using the FTS described in Refs. 17 and 18. Our FTS is operated at the Caltech Submillimeter Observatory on Mauna Kea, Hawaii, at an altitude of 4072 m. At this site, with a pressure 62% of that at sea level and a zenith precipitable H<sub>2</sub>O column abundance,  $N_{\text{H}_2\text{O}}$ , that is typically 5% of that at sea level,<sup>19</sup> foreign gas broadening of the H<sub>2</sub>O line shape is likely to dominate over effects that depend on the square of the water-vapor density (such as self-broadening and the possible opacity contributions of H<sub>2</sub>O dimers, clusters, and liquid aerosol particles), making interpretation more direct.

Better definition of the atmosphere's long-wave continuum opacity requires measurements with (1)

---

E. Serabyn and D. C. Lis are with the Department of Physics, California Institute of Technology, MS 320-47, Pasadena, California 91125. E. W. Weisstein is with the Department of Astronomy, University of Virginia, Charlottesville, Virginia 22903. J. R. Pardo is with the NASA Goddard Institute for Space Studies, 2880 Broadway, New York, New York 10025.

Received 12 February 1997; revised manuscript received 3 November 1997.

0003-6935/98/122185-14\$15.00/0

© 1998 Optical Society of America

broad frequency coverage, for which a FTS is the only practical instrument, (2) high signal-to-noise ratio, which our FTS's high throughput and sensitive 0.3-K detector<sup>17,18</sup> provide, (3) high calibration accuracy, the attainment of which is discussed extensively below, and (4) sampling over a large  $N_{\text{H}_2\text{O}}$  range to distinguish between effects of  $\text{H}_2\text{O}$  vapor and dry air. Here we describe our calibration procedures, present initial data covering the 0.9–0.3-mm wavelength range, and briefly discuss the implications of our spectra for the line-shape and quasi-continuum opacity issues, using the single-layer atmospheric transmission model, AT.<sup>20</sup>

## 2. Measurement and Calibration Procedures

Definition of the parameters of a broadband opacity requires both a wide frequency coverage ( $\geq$  factor of 3; Appendix A) and a spectral resolution fine enough to resolve narrow  $\text{O}_3$  lines from the continuum ( $\leq 1$  GHz). Our FTS meets both of these criteria (present range, approximately 175 GHz to 1 THz, or 1.7–0.3 mm; best resolution, 0.2 GHz), although currently a number of bandpass filters are required.<sup>17</sup> The root-mean-square spectral noise that results from a round-trip pair of FTS scans is roughly 1 K in brightness temperature units,<sup>18</sup> implying that a pair of scans on a typical Mauna Kea night sky of temperature 273 K should yield atmospheric transmission spectra with 3- $\sigma$  statistical noise levels of  $\approx 1\%$ . Calibration source temperatures are of comparable accuracy, implying that other systematic errors need to be kept below the 1% level as well. The exponent in a power-law continuum opacity can then be determined to an accuracy of  $\pm 0.1$  (Appendix A).

Rather than measuring the transmitted spectrum of a source above the atmosphere, we measure the sky's emission spectrum and convert it to transmission units by using Kirchhoff's law<sup>21</sup> (emissivity and absorptivity of a layer are equal in thermal equilibrium). We use this approach because the only (non-solar) submillimeter source adequately bright is the Moon, and its use would introduce limitations, such as limited access to its full phase, the need for accurate knowledge of the Moon's submillimeter brightness temperature distribution and coupling to the telescope, and the excessive duration needed for acquisition of transmission spectra over a range of air masses (necessary for determining the coupling to the source). To measure transmission quickly on any given night we thus use the alternative approach based on Kirchhoff's law. Conversion to a transmission scale then requires only a few additional calibration spectra, i.e., those of ambient and liquid  $\text{N}_2$  temperature blackbodies. The cold blackbody, a sheet of Eccosorb<sup>22</sup> AN-72 floating upon liquid  $\text{N}_2$ , is large enough to subtend the interferometer's entire input-side collimated beam.

Our calibration procedure is initially similar to the heterodyne approach,<sup>23,24</sup> so our initial description is brief. However, as differences arise because of the presence of frequencies in excess of the Rayleigh-Jeans regime, the broadband nature of the treat-

ment, the interferometric nature of FTS's, and the inclusion of a correction for differing ground and sky temperatures, we focus on these points in what follows. Measured interferograms are processed as in Ref. 17, and here we add only that the high signal strengths involved permit individual white-light fringe position determinations for the ambient, cold, and sky spectra.

With a dielectric-beam-splitter FTS,<sup>17</sup> elimination of Port 2 emission<sup>17,25</sup> requires difference spectra. Thus, with  $\nu$  the frequency and  $G(\nu)$  a combined optical-electrical gain factor, the difference voltage spectrum resulting from observation of ambient ground level and cold (liquid  $\text{N}_2$ ) temperature calibration blackbodies emitting power spectra  $P_g(\nu)$  and  $P_c(\nu)$ , respectively, is

$$V_g(\nu) - V_c(\nu) = G(\nu)\eta_c(\nu)[P_g(\nu) - P_c(\nu)]. \quad (1)$$

Here  $\eta_c(\nu)$  ( $= 1 - \text{reflectivity}$ ) is the coupling efficiency of the interferometer's beam to the cold load, and the reflected power is assumed to terminate on ambient temperature surfaces. On the other hand, differencing ambient temperature blackbody and sky spectra yields

$$V_g(\nu) - V_s(\nu) = G(\nu)[P_g(\nu) - (\eta_s(\nu)\{P_s(\nu) + \exp[-\tau_t(\nu)]P_b(\nu)\} + [1 - \eta_s(\nu)]P_g(\nu))]. \quad (2)$$

Here  $\eta_s(\nu)$  is the fraction of the spectrometer beam that reaches the sky<sup>23,24</sup> (the sky efficiency),  $P_s(\nu)$  is the sky emission spectrum,  $\tau_t(\nu)$  is the total opacity through the atmosphere in the observing direction at frequency  $\nu$ , and  $P_b(\nu)$  is the incident background spectrum. Equation (2) simplifies to

$$V_g(\nu) - V_s(\nu) = G(\nu)\eta_s(\nu)\{P_g(\nu) - P_s(\nu) - \exp[-\tau_t(\nu)]P_b(\nu)\}, \quad (3)$$

and division by Eq. (1) to eliminate  $G(\nu)$  yields a measured spectral ratio,  $m(\nu)$ , of

$$m(\nu) \equiv \frac{V_g(\nu) - V_s(\nu)}{V_g(\nu) - V_c(\nu)} = \frac{\eta_s(\nu) P_g(\nu) - P_s(\nu) - \exp[-\tau_t(\nu)]P_b(\nu)}{\eta_c(\nu) P_g(\nu) - P_c(\nu)}. \quad (4)$$

We now replace the various power spectra with blackbody-derived functions, allowing for the cancellation of the common instrumental étendue. For  $P_g$  and  $P_c$  we use blackbodies at ambient (ground level) and liquid  $\text{N}_2$  temperatures,  $T_g$  and  $T_c$ , respectively. We formally write the sky term as if the sky emission were isothermal, of effective temperature  $T_e$  and emissivity  $1 - \exp[-\tau_t(\nu)]$  [where  $\tau_t(\nu)$  remains the true total opacity]. The solution for  $T_e$  as a function of  $\nu$ , i.e., of  $\tau_t(\nu)$ , is given in Subsection 2.B. The background radiation term nominally consists of cosmic, galactic, and zodiacal contributions, but the two last named are negligible because of their low opacities: for large-scale galactic emission,<sup>26</sup>  $T < 22$  K and  $\tau < 5 \times 10^{-3}$  at  $\lambda > 350 \mu\text{m}$ ; for zodiacal emis-

sion,<sup>27</sup>  $T \approx 250$  K and  $\tau < 10^{-6}$ , so  $T\tau < 0.1$  K for both, implying possible transmission errors of  $< 0.03\%$ . A single background blackbody at  $T_b = 2.73$  K (Ref. 28) thus suffices, yielding

This equation permits the full expression for  $t(\nu)$  given in Eq. (7) to be recast as

$$t(\nu) = 1 - \left[ \frac{\exp(h\nu/kT_e) - 1}{\exp(h\nu/kT_g) - 1} \right] [1 - t_1(\nu)]. \quad (9)$$

$$m(\nu) = \frac{\left[ \frac{\eta_s(\nu)}{\eta_c(\nu)} \right] \frac{1}{\exp(h\nu/kT_g) - 1} \frac{1 - \exp[-\tau_t(\nu)]}{\exp(h\nu/kT_e) - 1} \frac{\exp[-\tau_t(\nu)]}{\exp(h\nu/kT_b) - 1}}{\frac{1}{\exp(h\nu/kT_g) - 1} - \frac{1}{\exp(h\nu/kT_c) - 1}}. \quad (5)$$

Solving algebraically for the atmospheric transmission spectrum,  $t(\nu) \equiv \exp[-\tau_t(\nu)]$ , then gives

$$t(\nu) = \frac{1 - \left[ \frac{\exp(h\nu/kT_e) - 1}{\exp(h\nu/kT_g) - 1} \right] \left\{ 1 - m(\nu) \frac{\eta_c(\nu)}{\eta_s(\nu)} \left[ 1 - \frac{\exp(h\nu/kT_g) - 1}{\exp(h\nu/kT_c) - 1} \right] \right\}}{1 - \frac{\exp(h\nu/kT_e) - 1}{\exp(h\nu/kT_b) - 1}}. \quad (6)$$

As the denominator of Eq. (6) differs from unity by  $\leq 0.1\%$  for  $\nu > 200$  GHz at  $T_e = 273$  K, the cosmic background can in fact also be neglected, yielding finally

$$t(\nu) = 1 - \left[ \frac{\exp(h\nu/kT_e) - 1}{\exp(h\nu/kT_g) - 1} \right] \times \left\{ 1 - m(\nu) \frac{\eta_c(\nu)}{\eta_s(\nu)} \left[ 1 - \frac{\exp(h\nu/kT_g) - 1}{\exp(h\nu/kT_c) - 1} \right] \right\}. \quad (7)$$

Equation (7) is our final calibration equation, in which conversion from  $m(\nu)$  to  $t(\nu)$  requires three temperatures and two coupling efficiencies. [The ratio in the first set of brackets could be replaced by  $T_g/T_e$  with only a slight loss of accuracy (Appendix B), but we prefer to retain full accuracy.] To make contact with simpler treatments, in the Rayleigh–Jeans limit with coupling efficiencies set to unity and  $T_e = T_g$ , Eq. (7) reduces to

$$t(\nu) = \left( \frac{T_g - T_c}{T_g} \right) \frac{V_g(\nu) - V_s(\nu)}{V_g(\nu) - V_c(\nu)}. \quad (7')$$

Continuing with the general case, we find a first-order approximation to  $t(\nu)$  in Eq. (7) by setting  $T_e = T_g$ , which yields

$$t_1(\nu) \equiv m(\nu) \frac{\eta_c(\nu)}{\eta_s(\nu)} \left[ 1 - \frac{\exp(h\nu/kT_g) - 1}{\exp(h\nu/kT_c) - 1} \right]. \quad (8)$$

Using Eq. (B3) of Appendix B for the ratio of two blackbody spectra of similar temperatures, we get

$$t(\nu) = 1 - \left[ 1 - \frac{\Delta T}{T_g} \frac{h\nu/kT_g}{1 - \exp(-h\nu/kT_g)} \right] [1 - t_1(\nu)], \quad (10)$$

where  $\Delta T \equiv T_e - T_g$ . Equation (10) can be rearranged into the more illuminating form

$$t(\nu) = t_1(\nu) + \frac{\Delta T}{T_g} \left[ \frac{h\nu/kT_g}{1 - \exp(-h\nu/kT_g)} \right] [1 - t_1(\nu)], \quad (11)$$

which illustrates that  $t(\nu)$  can be written as an expansion in the small quantity  $\Delta T/T_g$ , with  $t_1(\nu)$  the lowest-order term and

$$\Delta t(\nu) = \frac{\Delta T}{T_g} \left[ \frac{h\nu/kT_g}{1 - \exp(-h\nu/kT_g)} \right] [1 - t_1(\nu)] \quad (12)$$

the first correction term. The first factor in brackets accounts for deviations from the Rayleigh–Jeans case and is within 8.8% of unity for  $\nu < 1$  THz and  $T_g = 273$  K.

Equation (11) can also be inverted to read as

$$t_1(\nu) = t(\nu) - \frac{\Delta T}{T_g} \left[ \frac{h\nu/kT_g}{1 - \exp(-h\nu/kT_g)} \right] [1 - t(\nu)] \quad (13)$$

to first order in  $\Delta T/T_g$ . It is then immediately apparent that, in the  $t(\nu) = 1$  limiting case,  $t_1(\nu) = t(\nu) = 1$ , independently of  $\Delta T$ . On the other hand, for  $t(\nu) = 0$ , i.e., near the centers of strong absorption lines,  $t_1(\nu) = 0$  only if  $T_e \rightarrow T_g$  as the effective emission level sinks to ground level (see Subsection 2.B).

It is also apparent that in the normal case in which  $T_e \leq T_g$  (Subsection 2.B) we have  $t_1(\nu) \geq t(\nu)$ , so  $t_1(\nu)$  systematically overestimates the true transmission by a small amount.

The complete calibration procedure is then a two-step process. Initially the first-order solution  $t_1(\nu)$  is calculated by use of Eq. (8), i.e., under the  $T_e = T_g$  approximation. (This is roughly equivalent to the standard radio solution, except for its broadband applicability, the avoidance of the Rayleigh–Jeans approximation, and the explicit inclusion of a cold coupling factor.) At this stage the ratio  $\eta_s(\nu)/\eta_c(\nu)$  is needed (Subsection 2.A). In the second step the  $\Delta t(\nu)$  transmission correction [Eq. (12)] is added to  $t_1(\nu)$ , which requires an estimate for  $T_e(\nu)$ , i.e., for  $T_e[\tau_t(\nu)]$  (Subsection 2.B).

#### A. Coupling Efficiencies

In radio-style telescopes such as the Caltech Submillimeter Observatory, the sky efficiency, i.e., the coupling of the detector's beam to the sky, is typically somewhat less than unity,  $\eta_s \approx 0.9$ , because of losses such as secondary support-leg blockage and spillover past the primary and secondary edges. On the other hand, measurements<sup>29</sup> of the reflectivity of Eccosorb AN-72 indicate that, for a fairly wide range of incidence angles,  $\eta_c \approx 0.99$ .  $\eta_s$  is thus the more important factor, although both  $\eta_s$  and  $\eta_c$  need to be taken into account. In the narrow-band heterodyne case the sky coupling efficiency is determined from sky transmission measurements taken at several different zenith angles (termed a skydip), but in our case the frequency dependence of  $\eta_s(\nu)$  also emerges. However, the use of a two-beam interferometer brings an even more important advantage: Because only interferometrically modulated flux is detected in a rapid-scan FTS, an opaque pupil mask placed within the interferometer can raise the sky coupling efficiency to unity,<sup>17</sup> as interference occurs only for that portion of the detector's beam that passes through the unobscured portions of the mask to the sky. The net result is that  $\eta_s(\nu)/\eta_c(\nu) \approx 1.01$  and is relatively independent of frequency. Experimental verification of this result is presented in Section 3, but it should be clear that the  $\eta_s(\nu)/\eta_c(\nu)$  factor can be treated as a known quantity,  $\approx 1$ , once an initial skydip is performed.

To solve for the  $\eta_s(\nu)/\eta_c(\nu)$  and zenith opacity,  $\tau_{t,a=1}(\nu)$ , spectra we acquired transmission data at several air masses  $a_i$  and then first partially calibrated them with Eq. (8) by setting the unknown  $\eta_s(\nu)/\eta_c(\nu)$  term to unity. As a first approximation, the resultant  $t_1'(\nu) = t_1(\nu)\eta_s(\nu)/\eta_c(\nu)$  spectra could then be fitted to the linearized plane-parallel transmission equation

$$\ln[t_{a_i}'(\nu)] = \ln\left[\frac{\eta_s(\nu)}{\eta_c(\nu)}\right] - a_i\tau_{t,a=1}(\nu). \quad (14)$$

The best-fit solution to Eq. (14) at any given frequency provides the frequency-specific constants  $\eta_s(\nu)/\eta_c(\nu)$  and  $\tau_{t,a=1}(\nu)$ , and combining the solutions

for all  $\nu$  provides the best-fit  $\eta_s(\nu)/\eta_c(\nu)$  and  $\tau_{t,a=1}(\nu)$  spectra. Of course, once  $\eta_s(\nu)/\eta_c(\nu)$  is determined, a second, more direct solution for the zenith opacity spectrum is possible, as inserting  $\eta_s(\nu)/\eta_c(\nu)$  and  $a_i = 1$  back into Eq. (14) provides  $\tau_{t,a=1}(\nu)$  directly from the zenith transmission data alone. These two solutions for  $\tau_{t,a=1}(\nu)$  may differ if  $N_{\text{H}_2\text{O}}$  varies during the measurements or if the H<sub>2</sub>O layer is not quite plane parallel (e.g., if a mountaintop cap is present), or if other systematic errors are significant. A comparison of the two solutions thus provides a diagnostic for such errors.

#### B. Effective Sky Temperature

The specific intensity  $I_\nu$  that arrives at ground level from atmospheric emission in a given direction is given by the equation of radiative transfer as

$$I_\nu = \int_0^\infty B_\nu[T_s(z)]\exp[-\tau_z(\nu)]d\tau_z, \quad (15)$$

where  $B_\nu(T)$  is the Planck blackbody function (Appendix B),  $T_s(z)$  is the sky's physical temperature at altitude  $z$ , and  $\tau_z(\nu)$  is the opacity from ground level to altitude  $z$  in the observing direction. The total opacity through the atmosphere in the given direction,  $\tau_t(\nu)$ , is then  $\tau_{z \rightarrow \infty}(\nu)$ . On the other hand, it is simpler to describe the incoming radiation at any given  $\nu$  by blackbody emission of effective temperature  $T_e(\nu)$  and an opacity equal to the true  $\tau_t(\nu)$ , i.e.,

$$I_\nu = B_\nu[T_e(\nu)][1 - \exp(-\tau_t(\nu))]. \quad (16)$$

It is possible to solve for  $T_e(\nu)$  by equating Eqs. (15) and (16), yielding

$$B_\nu[T_e(\nu)] = \frac{1}{1 - \exp[-\tau_t(\nu)]} \int_0^\infty B_\nu[T_s(z)]\exp[-\tau_z(\nu)]d\tau_z. \quad (17)$$

To solve for  $T_e(\nu)$  we expand  $B_\nu[T_s(z)]$  about  $B_\nu[T_s(0)]$ , letting  $T_s(z) = T_s(0) + \Delta T_s(z)$ . To maintain generality we do not set  $T_s(0)$ , the atmospheric temperature at  $z = 0$ , equal to  $T_g$ , the ambient surface temperature. Thus

$$B_\nu[T_e(\nu)] = \frac{1}{1 - \exp[-\tau_t(\nu)]} \left\{ \int_0^\infty B_\nu[T_s(0)]\exp[-\tau_z(\nu)]d\tau_z + \int_0^\infty \left. \frac{dB_\nu[T_s(z)]}{dT} \right|_{z=0} \Delta T_s(z)\exp[-\tau_z(\nu)]d\tau_z \right\}. \quad (18)$$

Pulling the constants  $B_\nu[T_s(0)]$  and  $dB_\nu[T_s(z)]/dT|_{z=0}$  out of the integrals and using Eq. (B2) from Appendix B, we get

$$B_\nu[T_e(\nu)] = B_\nu[T_s(0)] + \frac{B_\nu[T_s(0)]}{T_s(0)} \times \left\{ \frac{h\nu/kT_s(0)}{1 - \exp[-h\nu/kT_s(0)]} \right\} \frac{1}{1 - \exp[-\tau_t(\nu)]} \times \int_0^\infty \Delta T_s(z) \exp[-\tau_z(\nu)] d\tau_z. \quad (19)$$

Dividing by  $B_\nu[T_s(0)]$  and applying Eq. (B3) for the ratio of two blackbody functions close in temperature then yields

$$T_e(\nu) = T_s(0) + \frac{1}{1 - \exp[-\tau_t(\nu)]} \times \int_0^\infty \Delta T_s(z) \exp[-\tau_z(\nu)] d\tau_z. \quad (20)$$

When the variable of integration is changed to  $z$ , Eq. (20) becomes

$$T_e(\tau_t) = T_s(0) + \frac{1}{1 - \exp(-\tau_t)} \times \int_0^\infty \Delta T_s(z) \exp(-\tau_z) \frac{d\tau_z}{dz} dz, \quad (21)$$

where for compactness the  $\nu$  dependencies of  $\tau_t$  and  $\tau_z$  have been suppressed. This general solution for  $T_e(\tau_t)$  then requires only specification of the vertical temperature and opacity profiles.

We now examine the case most likely to apply at high sites such as Mauna Kea. Because  $H_2O$  vapor is expected to dominate the opacities everywhere but in the immediate vicinity of a few strong  $O_2$  lines, we concentrate on  $H_2O$  opacities. The approximation of an exponential distribution of water vapor of scale height  $H$  should be a good one above the lower troposphere, implying that

$$\tau_z = \tau_t [1 - \exp(-z/H)]. \quad (22)$$

Note that the zenith angle does not appear explicitly but is implicit in  $\tau_t$ . Equation (22) in turn implies that  $d\tau_z/dz = (\tau_t/H) \exp(-z/H)$ . Furthermore,  $T_s(z)$  will be given at high altitudes to a good approximation by  $\Delta T_s(z) = -Lz$ , where  $L$  is a constant lapse rate  $\{L \equiv -[dT_s(z)]/dz\}$ , so

$$T_e(\tau_t) = T_s(0) - \frac{L}{H} \frac{\tau_t}{1 - \exp(-\tau_t)} \times \int_0^\infty z \exp(-z/H) \exp(-\tau_z) dz. \quad (23)$$

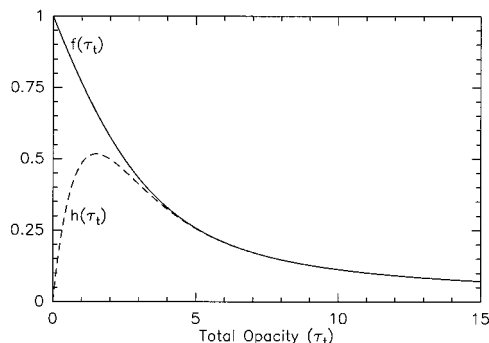


Fig. 1. Plots of the  $f(\tau_t)$  and  $h(\tau_t)$  functions defined by Eqs. (26) and (29). Multiplication of  $f(\tau_t)$  by  $LH$ , the temperature drop across an  $H_2O$  scale height, gives the departure of the sky's effective emission temperature from  $T_s(0)$  [Eq. (25)];  $h(\tau_t)$  serves an analogous role in calculation of  $\Delta t(\nu)$  [Eq. (28)].

When we change to the dimensionless variable  $s \equiv z/H$ , Eq. (23) becomes

$$T_e(\tau_t) = T_s(0) - LH \frac{\tau_t}{1 - \exp(-\tau_t)} \times \int_0^\infty s \exp(-s) \exp(-\tau_s) ds, \quad (24)$$

where now  $\tau_s = \tau_t [1 - \exp(-s)]$ . Thus

$$T_e(\tau_t) - T_s(0) = -LHf(\tau_t), \quad (25)$$

where

$$f(\tau_t) \equiv \frac{\tau_t}{1 - \exp(-\tau_t)} \int_0^\infty s \exp(-s) \times \exp\{-\tau_t[1 - \exp(-s)]\} ds. \quad (26)$$

The difference between  $T_e(\tau_t)$  and the ground-level air temperature  $T_s(0)$  thus depends only on the product of the temperature change,  $LH$ , across an  $H_2O$  scale height and on a dimensionless, analytical function of  $\tau_t$ . As  $\tau_t$  increases from 0 to  $\infty$  (i.e., as  $\nu$  varies appropriately), the falloff function  $f(\tau_t)$  decreases from 1 to 0 (Fig. 1), implying that  $T_e(\tau_t) \rightarrow T_s(0)$  as  $\tau_t$  increases. In general then,  $|T_e(\tau_t) - T_s(0)| \leq LH$ , with the maximum  $|T_e(\tau_t) - T_s(0)| = LH$  applying in the low-opacity limit. At the temperatures and pressures characteristic of Mauna Kea's summit, the appropriate theoretical value<sup>30</sup> for the saturated adiabatic lapse rate is  $5.6 \text{ K km}^{-1}$  (which the nearby Hilo, Hawaii, airport radiosonde data confirm), so  $|T_e(\tau_t) - T_s(0)| \leq 11.2 \text{ K}$  for  $H = 2 \text{ km}$ . On the other hand, as  $\tau_t \rightarrow \infty$ ,  $T_e(\tau_t) - T_s(0) \rightarrow -LH/\tau_t$ , so  $T_e(\tau_t)$  converges to  $T_s(0)$  at high  $\tau_t$ .

### C. $\Delta t(\nu)$ Correction Term

The quantity needed in Eq. (12) for the  $\Delta t(\nu)$  correction is  $\Delta T \equiv T_e - T_g$ , which from Eq. (25) is given by

$\Delta T = T_s(0) - T_g - LH f(\tau_t)$ . Inserting this into Eq. (12), we get

$$\Delta t(\nu) = \frac{T_s(0) - T_g - LHf(\tau_t)}{T_g} \frac{h\nu/kT_g}{1 - \exp(-h\nu/kT_g)} \times [1 - t_1(\nu)]. \quad (27)$$

Now, inasmuch as  $\Delta t(\nu)$  is a small correction term (because  $LH/T_g \approx 0.04$ ), it does not need to be determined accurately. Therefore  $t_1(\nu)$  in Eq. (27) can be replaced by  $\exp[-\tau_t(\nu)]$ . Furthermore, after the base of the atmosphere and the ground have equilibrated late at night, it is possible to set  $T_s(0) = T_g$  (a relation not applicable in general, e.g., immediately after sunrise), to yield

$$\Delta t(\nu) = -\frac{LH}{T_g} \frac{h\nu/kT_g}{1 - \exp(-h\nu/kT_g)} h(\tau_t), \quad (28)$$

where  $h(\tau_t)$ , the height function (essentially a weighting function), is

$$h(\tau_t) \equiv [1 - \exp(-\tau_t)]f(\tau_t) = \tau_t \int_0^\infty s \exp(-s) \exp\{-\tau_t[1 - \exp(-s)]\} ds, \quad (29)$$

which is also plotted in Fig. 1. As  $\max[h(\tau_t)] = 0.517$  at  $\tau_t \approx 1.5$  (Fig. 1), we have  $|\Delta t(\nu)| < 2.3\%$ . The largest absolute correction then occurs at midrange values of  $\tau_t$ , but the correction remains important across a wide opacity range, as transmission errors at low  $\tau_t$  are fractionally very important, whereas near the centers of moderately opaque lines, uncorrected transmissions  $t_1(\nu)$  will show slight offsets, because the  $H_2O$  line emission arises somewhat above ground level. In addition, because for extremely high  $\tau_t$  (i.e., at the bottoms of very opaque  $H_2O$  lines) we know that  $t(\nu) = 0$ , i.e.,  $t_1(\nu) + \Delta t(\nu) = 0$ , it follows that  $\Delta t = -t_1$  there. As  $f(\infty) = 0$ , Eq. (27) reduces to

$$\frac{T_s(0) - T_g}{T_g} = \frac{t_1}{t_1 - 1} \frac{1 - \exp(-h\nu/kT_g)}{h\nu/kT_g}. \quad (30)$$

Thus, if  $t_1(\nu) \neq 0$  at the bottoms of very opaque  $H_2O$  lines, it follows that  $T_s(0) \neq T_g$ . In this case we can still use Eq. (27) to calculate  $\Delta t(\nu)$ , determining the  $T_s(0) - T_g$  term first by applying Eq. (30) at the bottoms of very opaque  $H_2O$  lines.

Of course the procedure outlined does not correct  $O_2$  emission lines properly, as  $O_2$  has a larger scale height than  $H_2O$ , but a simple switch to a different scale height within the  $O_2$  lines yields the appropriate correction. Of course stratospheric  $O_3$  lines will also not be corrected properly, but that is unimportant in our primary application here.

### 3. Initial Results

Sky measurements with an appropriate Eccosorb pupil mask in the FTS were first carried out at the Caltech Submillimeter Observatory on the night of 6 February 1996, starting at UT 12:00, roughly coinci-

dent with the launch of the Hilo radiosonde. The observational field of view was 20 arcsec, and the frequency range was roughly 330 GHz–1 THz ( $\lambda \approx 0.9$ –0.3 mm). Four separate filters were used, identified in what follows by their approximate passband centers, 800, 600, 450, and 350  $\mu\text{m}$ . For each filter, four FTS scans (two in each direction) were obtained of the sky, as well as of the ambient and cold blackbodies, at each of four zenith angles spaced by 0.35 air mass. With a scan speed of 0.9–0.45 cm/s, a one-sided stage travel of 39.5 cm (yielding an unapodized spectral resolution of 0.23 GHz), and a significant overhead for numerous insertions of the cold load container, the observations took roughly 5 h to complete. Fits to the central frequencies of a number of narrow, isolated  $O_3$  lines yielded a root-mean-square frequency accuracy of 11 MHz, roughly one twentieth of a resolution element. At the shortest wavelengths and highest zenith angles, several of the scans were corrupted, as evidenced by nonzero, sloped baselines outside the atmospheric passbands [likely due either to slight atmospheric variations occurring during the higher-frequency measurements (see the next paragraph) or to the presence of some residual water vapor inside our open-air interferometer]. Excluding these scans from consideration, the uncorrupted data nevertheless include a zenith transmission spectrum covering the full 0.9–0.3-mm wavelength range and skydips covering the three upper zenith angles in the two lower-frequency filters. These scans permit a determination of  $\eta_s(\nu)/\eta_c(\nu)$  across the 330–550-GHz range.

The sky was crystal clear and stable during the observations. As shown by the weather logs (Fig. 2), the ambient temperature varied by  $<0.5$  K from its mean, 275.0 K, over the entire 5-h measurement interval. In addition, both the local humidity and the zenith opacity were quite constant, and the slight variations in these two parameters tracked each other well on this occasion. Regular estimates of the zenith opacity at 225 GHz were provided by an on-site heterodyne radiometer<sup>31</sup> (termed the taumeter), and these  $\tau_{225}$  readings were rather low during our measurements [Fig. 2(c)]. However, as the taumeter's absolute calibration was likely in error by approximately 30–50% during 1996, we unfortunately cannot use the taumeter readings quantitatively. However, we can use them to track time variations. On this basis [Fig. 2(c)] we can see that the atmospheric opacity was stable to  $\pm 1.4\%$  between scans 80 and 170. This stable period included our skydips with the 800- and 600- $\mu\text{m}$  filters and the 450- $\mu\text{m}$  zenith data. The earlier scans in the data set (1–79) corresponded to a marginally ( $\sim 3\%$ ) higher  $\tau_{225}$ , the ramifications of which are addressed below.

Figure 3(a) presents the combined results of our skydips in the two longest-wavelength (800- and 600- $\mu\text{m}$ ) filters, calibrated to the  $t_1(\nu)$  scale with Eq. (8), with  $\eta_s(\nu)/\eta_c(\nu)$  initially set to unity. This subset of the measurements was completed entirely within the 2-h stable interval noted. The best-fit  $\eta_s(\nu)/\eta_c(\nu)$  spectrum resulting from fitting Eq. (14) to this data

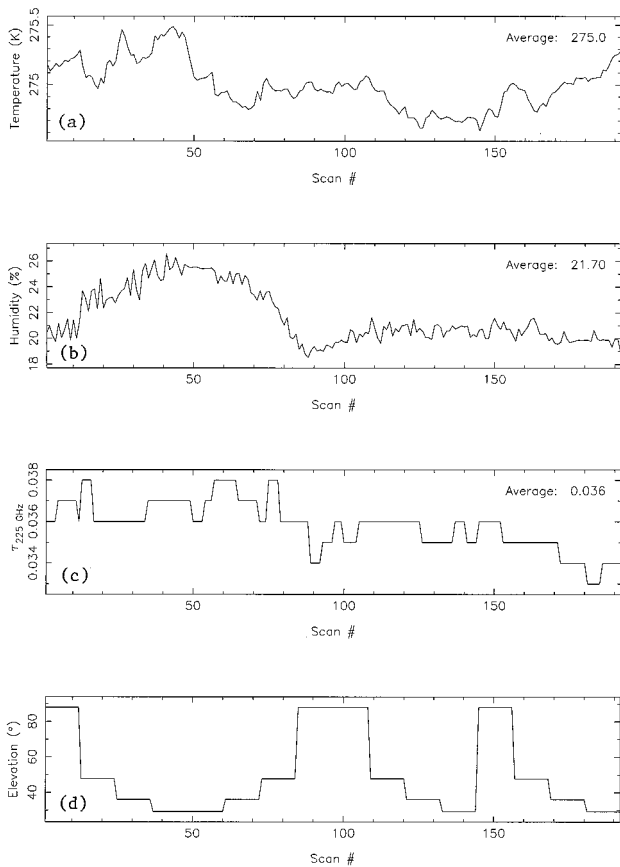


Fig. 2. Weather logs for 6 February 1996 versus scan number: (a) Ambient temperature. (b) Local humidity. (c) Zenith opacity at 225 GHz provided by the taumeter. The absolute calibration is likely low by approximately 30–50%, but time variations are accurately reflected in the data. (d) Telescope elevation angle. Four skydips corresponding to the four filters can be discerned in the order 350, 450, 800, and 600  $\mu\text{m}$ .

set is plotted as a solid histogram in Fig. 3(b), binned to 2-GHz resolution to improve the signal-to-noise ratio. It reveals that, as expected,  $\eta_s(\nu)/\eta_c(\nu) \approx 1.01$  across most of the observed band, except near opaque lines and the high-frequency band edge, where the atmospheric transmission plummets. On application of the  $\Delta t(\nu)$  correction to these data, the fitted  $\eta_s(\nu)/\eta_c(\nu)$  curve improves markedly near the band edge [dashed-dotted histogram in Fig. 3(b)], thus verifying the need for the higher-order  $\Delta t(\nu)$  correction in regions of high opacity. Systematic errors can be gauged by differencing of the corrected zenith transmission data and the zenith transmission derived from the fit to the full skydip data set, and, as Fig. 3(c) shows, the systematic residuals are  $\lesssim 2\%$ . On correction for  $\eta_s(\nu)/\eta_c(\nu)$  and  $\Delta t(\nu)$ , the skydip data are thus quite consistent with both a stable atmosphere and the plane-parallel assumption. Finally, note that the transmission levels near the centers of the most opaque  $\text{H}_2\text{O}$  lines (at 380, 448, and 557 GHz) are zero to within the noise (1% or so), signaling that the  $T_s(0) = T_g$  condition was satisfied.

The remaining two zenith spectra, in the 450- and

350- $\mu\text{m}$  filters, are plotted in Fig. 4. We reduced these spectra by assuming for now that  $\eta_s/\eta_c = 1.01$ , as at lower values of  $\nu$ . Of the two high- $\nu$  spectra, the 450- $\mu\text{m}$  spectrum was acquired at the start of the 2-h stable period during which the lower-frequency data were acquired; thus all data below 750 GHz can be considered as representing the same sky conditions. On the other hand, the 350- $\mu\text{m}$  data were acquired 3 h before the other data, so these data may correspond to slightly different atmospheric conditions. Nevertheless, according to Fig. 2 the opacity and humidity at the start of the observations were quite similar to those present during the later stable period, and the change in  $\tau_{225}$  over the full 5-h period was only  $\approx 3\%$ , which corresponds to  $\Delta\tau(850 \text{ GHz}) \approx 0.03$  for  $\tau(850 \text{ GHz}) \approx 1$ . This in turn corresponds to a possible 850-GHz transmission error of only  $\approx 1\%$ , or an error in the continuum opacity frequency power-law exponent (Appendix A) of only several hundredths, and so can be ignored hereafter. In these high-frequency windows the  $\Delta t$  correction term is  $\approx 2\%$ , whereas 3- $\sigma$  random errors decrease from  $\approx 2\%$  at  $\nu < 550$  GHz to 0.6% for  $\nu > 550$  GHz, implying that the  $\Delta t$  correction is a necessity at the higher frequencies.

The final, fully calibrated zenith transmission and opacity spectra for the night of 6 February 1996, combining the  $\Delta t$ -corrected zenith spectra in all four filters, are presented in Fig. 5(a). Note that most of the opaque lines now correctly bottom out quite close to zero, as a result of the slight second-order correction. All the spectral lines that appear in Figs. 3–5 have been identified with the aid of the Jet Propulsion Laboratory line catalog.<sup>32</sup> The broad lines labeled in Fig. 5(a) are all attributable to absorption by  $\text{O}_2$ ,  $\text{H}_2\text{O}$ ,  $\text{HDO}$ , and vibrationally excited  $\text{H}_2\text{O}$ , whereas the many weak and narrow lines seen are almost entirely attributable to  $\text{O}_3$ . Weak evidence for  $\text{O}^{18}\text{O}$  is also present [Fig. 4(b)], but this molecule was better seen in our preliminary low-frequency data.<sup>33</sup>

The opacity spectrum in Fig. 5(b) is presented normalized by  $\tau(345)$  to provide a quantity that is relatively independent of  $N_{\text{H}_2\text{O}}$ . Of perhaps more interest is the ratio  $\tau(\nu)/\tau(225)$ , which would allow conversion of calibrated 225-GHz taumeter readings to submillimeter opacity curves, assuming stability in the meteorological profiles. As our measurements did not extend to 225 GHz, this step must await reconfiguration of the FTS filters, but our best model fits (Section 4) yield a scaling factor,  $\tau(345)/\tau(225)$ , of  $\approx 3.15 \pm 0.25$ , in good accord with earlier estimates.<sup>34,35</sup>

#### 4. Model Calculations

As an initial step in analyzing our data, the atmospheric opacity model AT<sup>20</sup> was employed. This model first calculates an effective temperature and pressure for each atmospheric constituent and then calculates opacities for the resultant layers. AT allows for a selection of analytical collisionally broadened line profiles but does not provide any continuum

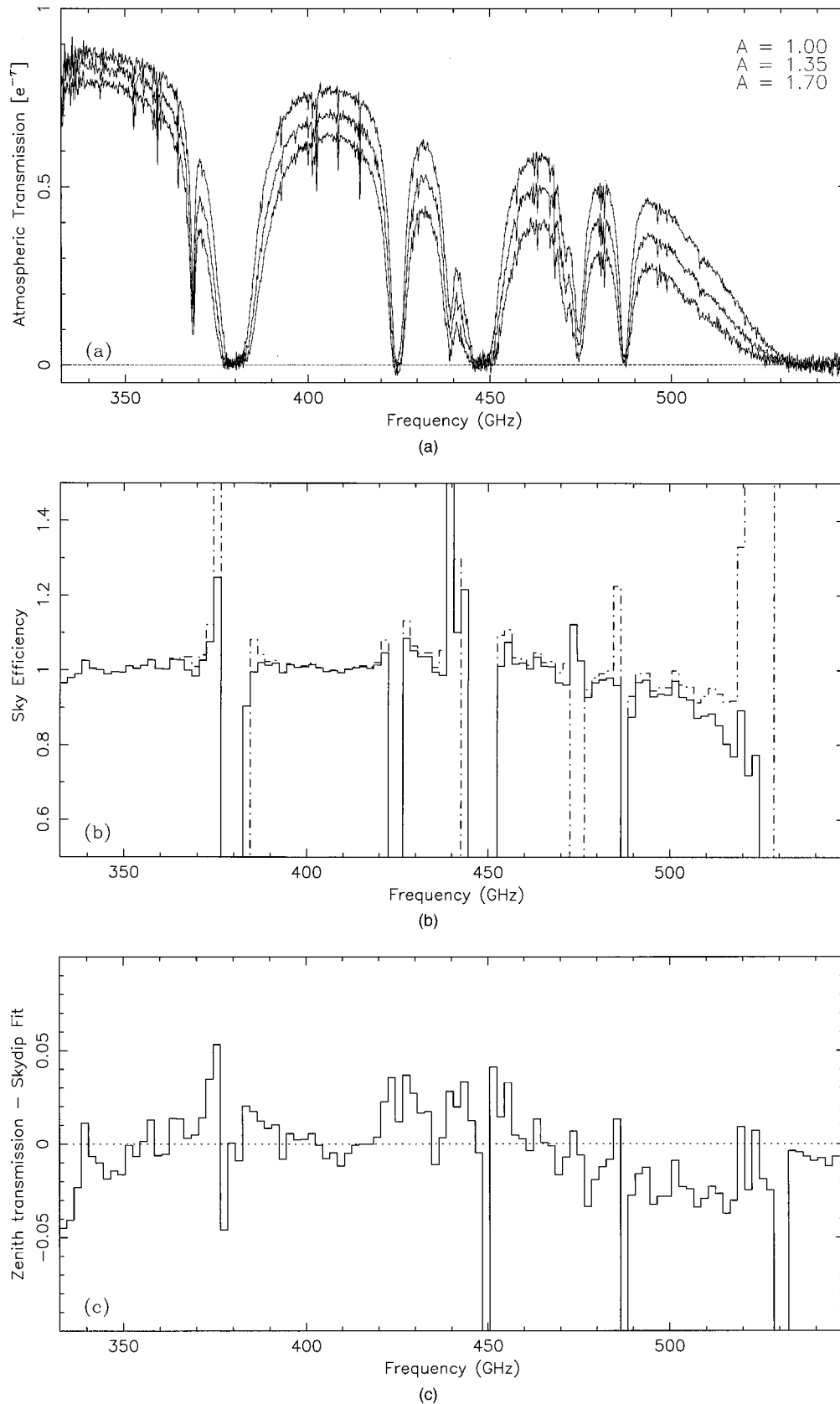


Fig. 3. (a) Atmospheric transmission spectra  $t_1(\nu)$  measured with the 800- and 600- $\mu\text{m}$  filters for telescope zenith angles corresponding to air masses of 1.00, 1.35, and 1.70 (curves from top to bottom). The spectral resolution for these and all subsequent data is 0.23 GHz. (b) Best fit  $\eta_s(\nu)/\eta_c(\nu)$  efficiency for the data of (a) binned to a resolution of 2 GHz (solid histogram) and the same after the  $\Delta t(\nu)$  correction has been added (dashed-dotted histogram). (c) Difference between the corrected zenith transmission spectrum,  $t(\nu)$ , and the best-fit zenith transmission derived from a fit to the full skydip data set.

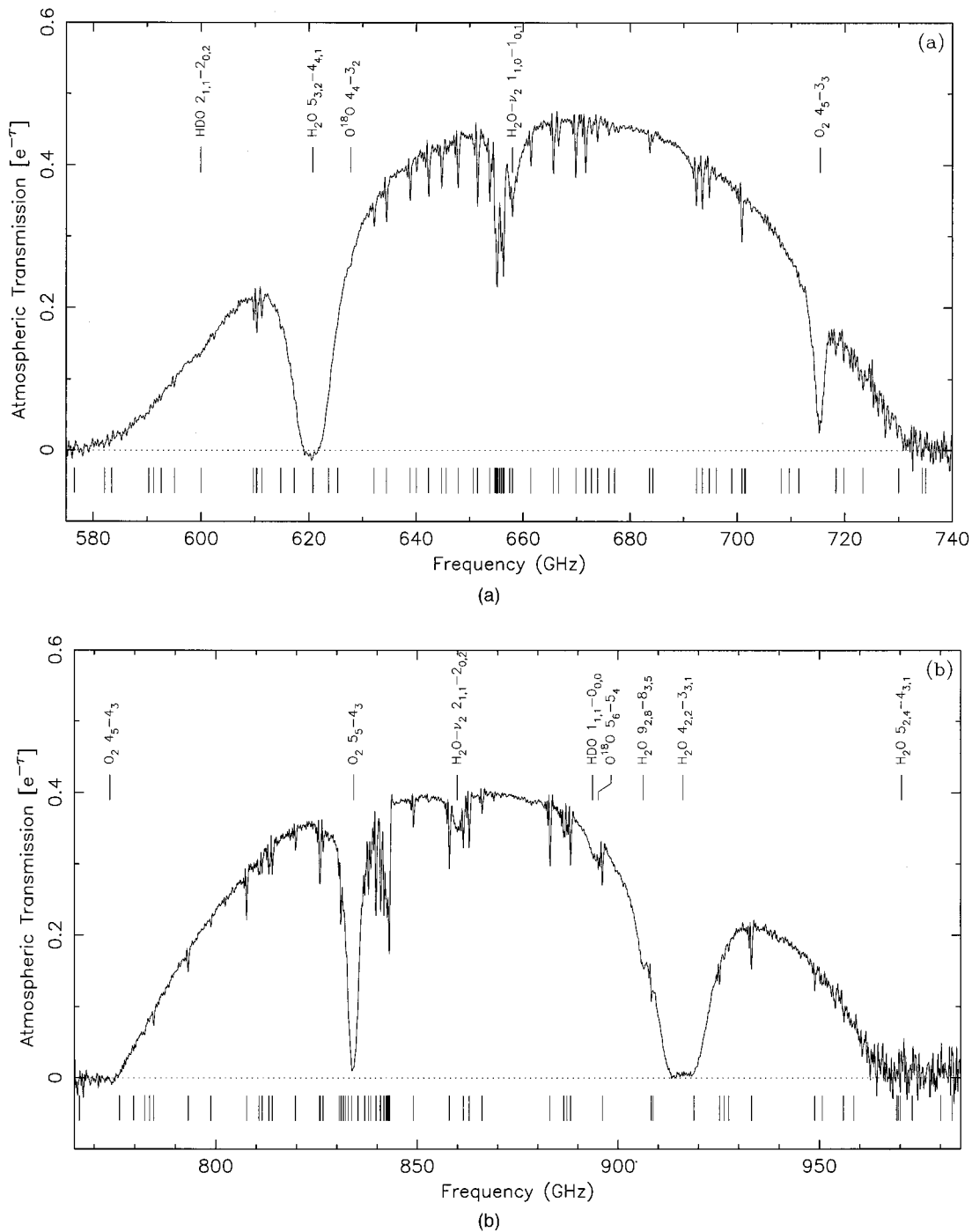


Fig. 4. (a) Measured  $t_1(\nu)$  transmission spectra in (a) the 450- $\mu\text{m}$  atmospheric window, (b) the 350- $\mu\text{m}$  atmospheric window. The positions of the stronger O<sub>3</sub> lines are marked with ticks just below the zero level. Some ringing is present because no apodization was applied.

opacity term. As a result, AT does not fit the continuum transmission level far from the line centers well.<sup>20</sup> To reproduce our transmission spectra better, we augmented AT's line sum opacity by a frequency power-law continuum opacity<sup>3-6</sup> given in terms of  $N_{\text{H}_2\text{O}}$ , a coefficient  $S$ , and an exponent  $\alpha$  by

$$\tau_c(\nu) = S \left( \frac{\nu}{\nu_0} \right)^\alpha N_{\text{H}_2\text{O}}, \quad (31)$$

where  $\nu_0$  is a reference frequency (here 225 GHz). Note that  $N_{\text{H}_2\text{O}}$  is determined from the observed H<sub>2</sub>O line cores, whereas the two power-law parameters are determined from the residual opacity between the lines, so, in contrast to narrow-band measurements, broadband FTS spectra independently provide both  $N_{\text{H}_2\text{O}}$  and the continuum opacity. Note also that at this early stage in our program we make no attempt to separate out a dry-air continuum opacity, as we

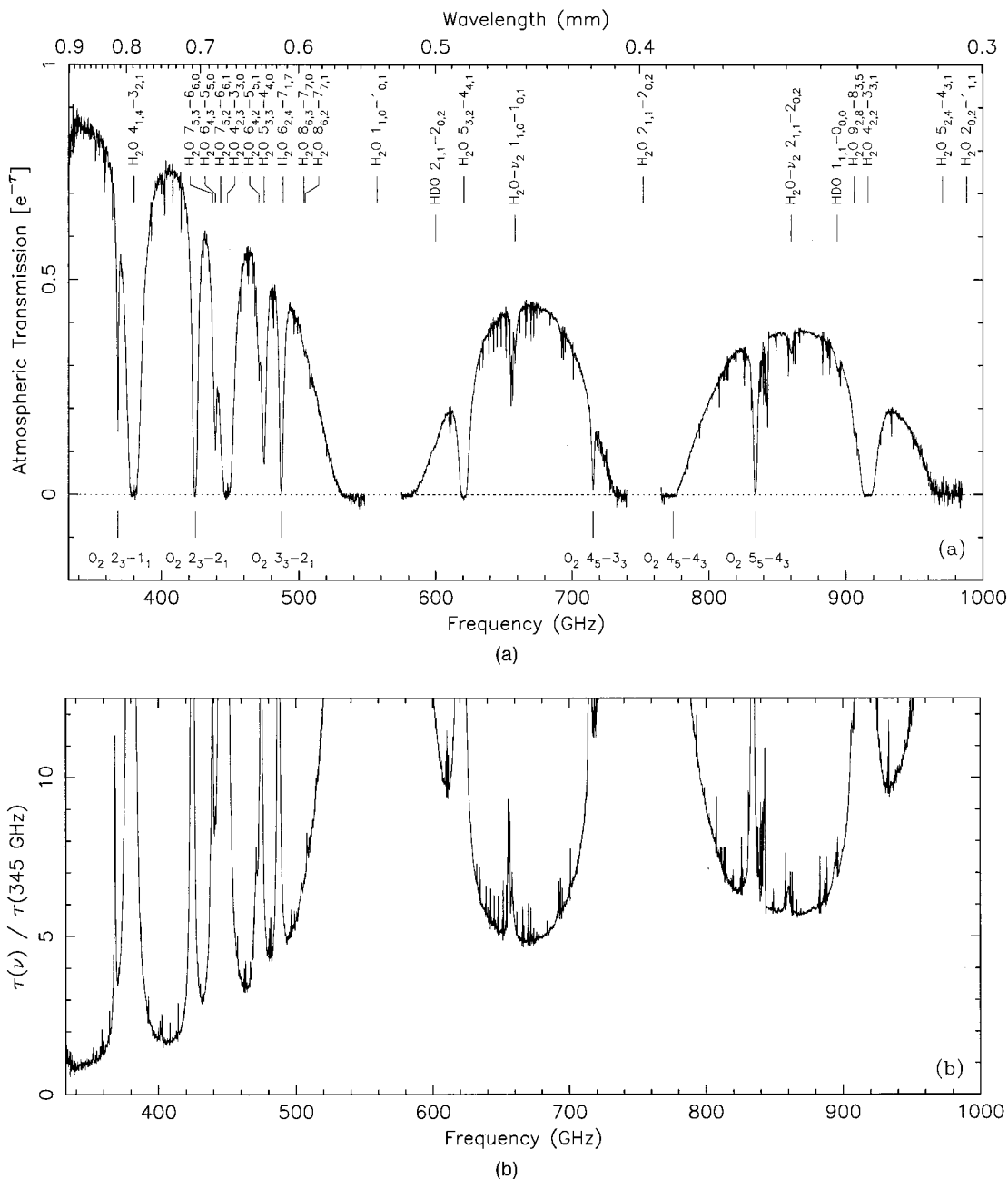


Fig. 5. (a) Combined fully calibrated  $t(\nu)$  zenith transmission spectrum covering the 333–985-GHz range, with all broad lines (from H<sub>2</sub>O, HDO, and O<sub>2</sub>) identified. (b) Corresponding zenith opacity spectrum, normalized by the 345-GHz opacity.

have data for only one H<sub>2</sub>O column. Thus we expect our model parameters to undergo some future revision.

To match the measured spectra we searched the three-dimensional parameter space defined by  $N_{\text{H}_2\text{O}}$ ,  $S$ , and  $\alpha$  for the best overall fit to the data by means of a  $\chi^2$  minimization. This fitting procedure was carried out for two line profiles—the van Vleck–Weisskopf and the kinetic (i.e., harmonic oscillator, Gross, or Zhevakin–Naumov) profiles—the first goal being merely to establish how well these profiles fit the data on inclusion of an empirical continuum. However, before we carried out this fitting procedure

we found it necessary to lower the model O<sub>3</sub> concentration by ~37% to avoid having  $\chi^2$  reflect errors in the O<sub>3</sub> concentration rather than the three parameters of interest. Because our calibration is not expected to treat the cooler O<sub>3</sub> layer accurately, and because the observed and model O<sub>3</sub> linewidths also disagree somewhat, we do not address O<sub>3</sub> further here.

We then carried out fits as described above for several subsets of the data to determine the sensitivity of the fitted parameters to the input data. When we count the combined 800–600- $\mu\text{m}$  data [Fig. 3(a)] as single spectra, our data set then consists of five

Table 1. Model Results for van Vleck–Weisskopf and Kinetic Line Shapes

Model Number	$N_{\text{H}_2\text{O}}$ (mm)	Coefficient ( $S$ )	Exponent ( $\alpha$ )	$\tau(225)$	Notes
van Vleck–Weisskopf					
1a	0.74	0.056	1.65	0.057	5 sets
2a	0.76	0.058	1.45	0.060	4 sets (no 350 $\mu\text{m}$ )
3a	0.76	0.051	1.65	0.054	3 sets (zenith)
4a	0.74	0.053	1.75	0.055	3 sets (no 350–450 $\mu\text{m}$ )
5a	0.76	0.064	1.35	0.064	2 sets (800–450- $\mu\text{m}$ zenith)
6a	0.76	0.045	1.75	0.050	2 sets (450–350- $\mu\text{m}$ zenith)
7a	0.74	0.045	1.90	0.053	1 set (800- $\mu\text{m}$ zenith)
Kinetic					
1b	0.72	0.036	2.00	0.048	5 sets
2b	0.72	0.035	2.05	0.047	4 sets (no 350 $\mu\text{m}$ )
3b	0.76	0.030	2.00	0.046	3 sets (zenith)
4b	0.72	0.051	1.35	0.058	3 sets (no 350–450- $\mu\text{m}$ )
5b	0.74	0.034	2.00	0.047	2 sets (800–450- $\mu\text{m}$ zenith)
6b	0.80	0.028	1.90	0.046	2 sets (450–350- $\mu\text{m}$ zenith)
7b	0.74	0.056	1.05	0.064	1 set (800- $\mu\text{m}$ zenith)

individual spectra: three at  $\nu < 550$  GHz [the skydip of Fig. 3(a)] and the 450- and 350- $\mu\text{m}$  zenith spectra (Fig. 4). For the fitting, these spectra were combined as follows, in decreasing numbers of spectra: (1) all five spectra, (2) the four spectra at  $\nu < 750$  GHz (i.e., excluding the 350- $\mu\text{m}$  spectrum), (3) the three spectra making up the full-frequency zenith spectrum [Fig. 5(a)], (4) the three low-frequency spectra (the  $\nu < 550$ -GHz skydip), (5) the two zenith spectra at  $\nu < 750$  GHz, (6) the two high-frequency zenith spectra at  $\nu > 550$  GHz, and (7) the low-frequency zenith spectrum alone.

The results for the best-fit  $N_{\text{H}_2\text{O}}$ ,  $S$ , and  $\alpha$  for the cases listed are given in Table 1 for both the van Vleck–Weisskopf and the kinetic line profiles. It is clear from Table 1 that, independently of the choice of line profile or of the subset of the data selected, the best determined parameter is  $N_{\text{H}_2\text{O}} \approx 0.74$  mm. The remaining parameters are not quite so well constrained.  $S$  is reasonably well constrained for a given choice of line shape but differs between the two line profiles. On the other hand,  $\alpha$  shows a large scatter for the smaller data subsets and yields a reproducible value only when a large enough data base, in terms either of frequency range or zenith angle (either of which corresponds to a large range in opacity), is included (models 1–3). For models 1–3 the van Vleck–Weisskopf profile calls for an  $\alpha$  somewhat less than 2 (average,  $\approx 1.6$ ), whereas the kinetic profile calls for  $\alpha \approx 2$ . The kinetic profile thus calls for a continuum opacity steeper by  $\approx 0.4$  in  $\alpha$ . However, we note that  $\alpha$  may itself depend on  $N_{\text{H}_2\text{O}}$  as the submillimeter region may be closer to a far-wing situation for low  $N_{\text{H}_2\text{O}}$  but to a near-wing case for high  $N_{\text{H}_2\text{O}}$ .

These results for  $\alpha$  are reasonably consistent with our earlier preliminary results<sup>33</sup> if the correct comparison is made. Inasmuch as the earlier data covered only the  $\nu < 550$  GHz range, our models 4 and 7 are the closest analogs, and for these the best-fit  $\alpha$  for the kinetic profile is lower than for the van Vleck–Weisskopf profile, as in the earlier case.<sup>33</sup> However,

these results conflict with our full-frequency models (1–3), which yield a higher  $\alpha$  for the kinetic case, thus underscoring the need for a large frequency range to determine  $\alpha$  reliably. This condition applies especially for the kinetic case, as its more prominent low-frequency far-wing opacity better masks additional opacity contributions.

Our best fits to the full zenith spectrum (model 3) and the corresponding residuals are shown in Fig. 6 for both line profiles. It is clear that either line profile can be combined with a power-law continuum to fit our data to the level of a few percent. However, slight differences are evident:  $\chi^2$  is typically  $\approx 25\%$  lower for the van Vleck–Weisskopf profile and Fig. 6 suggests small systematic differences at high  $\nu$ . In particular, the steeper continuum that accompanies the kinetic profile yields more asymmetric high-frequency  $\text{H}_2\text{O}$  lines and intervening atmospheric windows for this case, leading to larger slopes in the residuals (Fig. 6). On the other hand, the kinetic profile seems to provide a slightly better match to the transmission levels at the centers of both high-frequency windows and yields an  $\alpha$  more in accord with the most commonly assumed<sup>3,5</sup> value of 2. Although it is thus premature to favor either profile, the current data do suggest that one of these profiles may eventually prove more fitting, at least in the context of an empirical continuum.

## 5. Conclusions and Prospects

Although these initial results establish the necessary experimental procedures and resultant accuracy, further measurements are clearly needed to provide a broader data base. Several instrumental and modeling improvements can ease the task. It is of course critical to speed up the process, to come as close as possible to snapshot measurements. This can be done easily with broader filters, although elimination of the need for skydips by measuring  $\eta_s/\eta_c$  also shortens the measurement time by a large factor. Thus an eventual on-sky time of several minutes is feasible. Extending the measurement range to lower fre-

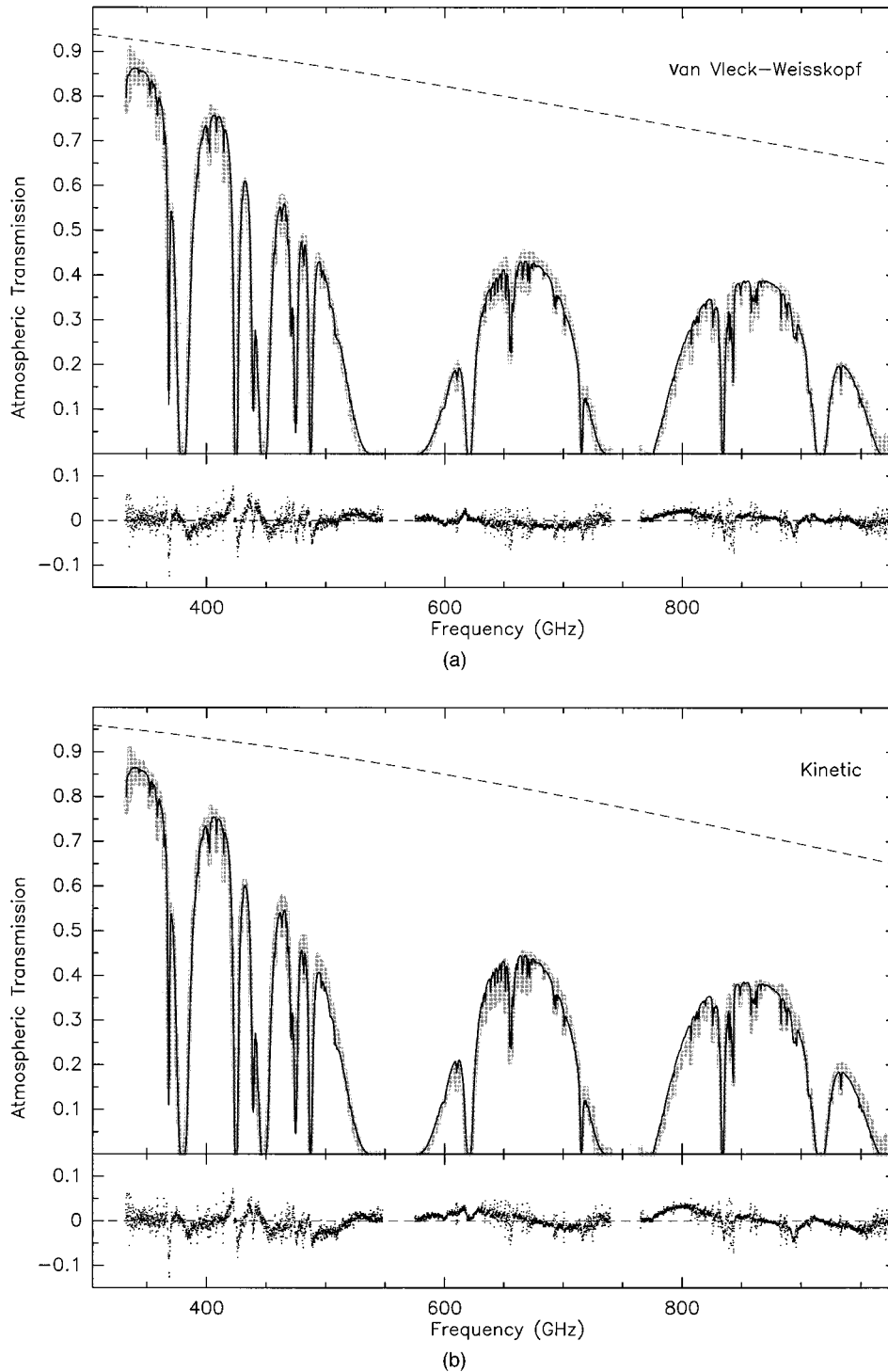


Fig. 6. Best-fit zenith transmission models (thin, dark curves) superposed upon the measured  $t(\nu)$  spectra (plotted as light-gray bands, the widths of which represent average error bars) for the (a) van Vleck–Weisskopf and (b) kinetic line profiles. The best-fit empirical continua included for the two cases are plotted above the model spectra, and their parameters are given in Table 1 (models 3a and 3b, respectively). The residuals between the data and models are given in the smaller panels below the spectra on the same vertical scale. The narrow spikes in the residuals correspond mostly to  $O_2$  and  $O_3$  lines.

quencies will also be vital, in particular because inclusion of the less-saturated 183- and 325-GHz  $H_2O$  lines will permit direct inversion for the  $H_2O$  vertical profile, knowledge of which will be vital in achieving higher accuracy in the analysis.

In the long run, our aim is to compile a database of atmospheric spectra covering a wide range of  $N_{H_2O}$ . Ultimately there are three goals for the intended measurements. First, it will permit experimental separation of the wet and dry continuum opacity com-

ponents. Second, with a sufficient database it should become possible to predict accurately the current sub-millimeter transmission spectrum from an accurate measurement of atmospheric opacity at a single frequency (such as 225 GHz) if the relevant meteorological parameters (e.g., the H<sub>2</sub>O scale height) are stable. Crude extrapolations from 225 GHz to higher frequencies are already possible, but this procedure remains rather uncertain in the face of sparse data and a 225-GHz opacity sometimes low enough to make small systematic errors important (thus a higher or dual-frequency monitor would better fulfill this role). Third, both empirical and quantum calculations are beginning to yield more-suitable H<sub>2</sub>O collisionally broadened far-wing opacities,<sup>8–10</sup> and a detailed comparison of an expanded suite of FTS measurements with such models will likely prove illuminating.

#### Appendix A. Systematic Uncertainties in the Determination of the Exponent $\alpha$

From Eq. (31), the derivative of the continuum opacity  $\tau_c(\nu)$  with respect to the exponent  $\alpha$  is

$$\frac{d\tau_c}{d\alpha} = SN_{\text{H}_2\text{O}} \left(\frac{\nu}{\nu_0}\right)^\alpha \ln\left(\frac{\nu}{\nu_0}\right) = \tau_c(\nu) \ln\left(\frac{\nu}{\nu_0}\right). \quad (\text{A1})$$

Converting to transmission,  $t(\nu)$ , using  $\tau(\nu) = -\ln[t(\nu)]$  and  $d\tau = -dt/t(\nu)$ , then implies that

$$d\alpha = \frac{dt}{t(\nu) \ln[t(\nu)] \ln\left(\frac{\nu}{\nu_0}\right)}. \quad (\text{A2})$$

With  $\nu_0$  and  $\nu$  the two frequency extremes, the uncertainty  $d\alpha$  is clearly minimized by maximization of the measurement range (although the gain in accuracy once  $\nu/\nu_0 > e$  is not rapid). Furthermore, as  $t(\nu) \ln[t(\nu)]$  has a maximum absolute value of  $e^{-1}$  at  $t = e^{-1}$ , the ultimate accuracy limit is

$$d\alpha \geq \frac{edt}{\ln\left(\frac{\nu}{\nu_0}\right)}. \quad (\text{A3})$$

For an accuracy  $d\alpha \approx 0.1$ , the minimum frequency span required is then  $\nu/\nu_0 = 1.3$  for  $dt = 0.01$ , and  $\nu/\nu_0 = 1.7$  for  $dt = 0.02$ . Of course, departures of  $t(\nu) \ln[t(\nu)]$  from its maximum degrade  $d\alpha$  further, so a more practical minimum is  $\nu/\nu_0 \geq 3$ .

In our current data set, at high frequencies  $t(\nu) \approx 0.4$  and  $\ln[t(\nu)] \approx -1$ , and systematic errors are of the order of  $dt \approx \pm 0.02$ , yielding  $d\alpha \approx \pm 0.05$ . On the other hand, at the low  $\nu$  end of our spectrum,  $t(\nu) \approx 0.87$ ,  $\ln[t(\nu)] \approx -0.13$ , and  $dt \approx \pm 0.01$ , so  $d\alpha \approx \pm 0.1$ . Thus, because high transmissions at low frequencies translate to small opacities, which necessarily have larger fractional errors, it is the low frequencies that dominate the uncertainty in  $\alpha$ .

#### Appendix B. Ratios of Blackbody Spectra of Similar Temperatures

Because the Planck blackbody function  $B_\nu(T)$  is given by

$$B_\nu(T) = \frac{2h\nu^3/c^2}{\exp(h\nu/kT) - 1}, \quad (\text{B1})$$

its derivative can be written as

$$\frac{dB_\nu}{dT} = \frac{B_\nu}{T} \frac{h\nu/kT}{1 - \exp(-h\nu/kT)}. \quad (\text{B2})$$

For small changes in temperature from an initial  $T_0$  the ratio of two blackbody functions of similar temperature can then be approximated as

$$\frac{B_\nu(T)}{B_\nu(T_0)} = 1 + \frac{T - T_0}{T_0} \left[ \frac{h\nu/kT_0}{1 - \exp(-h\nu/kT_0)} \right]. \quad (\text{B3})$$

If  $h\nu/kT$  is also small, the term in brackets can be expanded, yielding

$$\begin{aligned} \frac{B_\nu(T)}{B_\nu(T_0)} &= 1 - \frac{T - T_0}{T_0} \left( 1 + \frac{h\nu}{2kT_0} \right) \\ &= 1 - \frac{T - T_0}{T_0} - \frac{T - T_0}{T_0} \left( \frac{h\nu}{2kT_0} \right). \end{aligned} \quad (\text{B4})$$

The first non-Rayleigh–Jeans correction term to  $B_\nu(T)/B_\nu(T_0)$  is thus  $[(T - T_0)/T_0][h\nu/(2kT_0)]$ . Now for  $T_0 = T_g = 273$  K and  $\nu < 1$  THz, we get  $h\nu/2kT_g < 0.088$ . At the same time, for  $LH = 11.2$  K (Subsection 2.B), we get  $T_e - T_g/T_g < 0.04$ , implying that the first non-Rayleigh–Jeans correction term in Eq. (B4) is  $< 0.35\%$  across the submillimeter region. Using Eq. (B4), one could then simplify Eq. (7) to read as

$$t(\nu) = 1 - \frac{T_g}{T_e} \left\{ 1 - m(\nu) \frac{\eta_c(\nu)}{\eta_s(\nu)} \left[ 1 - \frac{\exp(h\nu/kT_g) - 1}{\exp(h\nu/kT_e) - 1} \right] \right\} \quad (\text{B5})$$

with a comparable loss in accuracy.

This study was supported by National Science Foundation grants AST96-15025 and ATM-9616766. We thank T. G. Phillips for a critical reading of the manuscript and R. R. Gamache and A. Bauer for helpful discussions.

#### References and Notes

1. W. A. Traub and M. T. Stier, "Theoretical atmospheric transmission in the mid- and far-infrared at four altitudes," *Appl. Opt.* **15**, 364–377 (1976).
2. A. Deepak, T. D. Wilkerson, and L. H. Ruhnke, *Atmospheric Water Vapor* (Academic, New York, 1980).
3. J. W. Waters, "Absorption and emission by atmospheric gases," in *Methods of Experimental Physics 12B: Astrophysics*, M. L. Meeks, ed. (Academic, New York, 1976), pp. 142–176.
4. D. P. Rice and P. A. R. Ade, "Absolute measurements of the atmospheric transparency at short millimetre wavelengths," *Infrared Phys.* **19**, 575–584 (1979).
5. H. J. Liebe, "An atmospheric millimeter-wave propagation model," *Int. J. Infrared Millimeter Waves* **10**, 631–650 (1989).

6. P. W. Rosenkranz, "Absorption of microwaves by atmospheric gases," in *Atmospheric Remote Sensing by Microwave Radiometry*, M. A. Janssen, ed. (Wiley, New York, 1993), pp. 37–79.
7. W. B. Grant, "Water vapor absorption coefficients in the 8–13- $\mu\text{m}$  spectral region: a critical review," *Appl. Opt.* **29**, 451–462 (1990).
8. P. W. Rozenkranz, "Pressure broadening of rotational bands. I. A statistical theory," *J. Chem. Phys.* **83**, 6139–6144 (1985).
9. S. A. Clough, F. X. Kneizys, R. W. Davies, "Line shape and the water vapor continuum," *Atmos. Res.* **23**, 229–241 (1989).
10. Q. Ma and R. H. Tipping, "Water vapor continuum in the millimeter spectral region," *J. Chem. Phys.* **93**, 6127–6139 (1990).
11. H. J. Liebe, "The atmospheric water vapor continuum below 300 GHz," *Int. J. Infrared Millimeter Waves* **5**, 207–227 (1984).
12. R. L. de Zafra, M. Jamarillo, J. Barrett, L. K. Emmons, A. Parrish, and P. M. Solomon, "Measurement of atmospheric opacity at 278 GHz at McMurdo station, Antarctica in austral spring seasons, 1986 and 1987," *Int. J. Infrared Millimeter Waves* **11**, 463–467 (1990).
13. R. A. Chamberlin and J. Bally, "225-GHz atmospheric opacity of the South Pole sky derived from continual radiometric measurements of the sky-brightness temperature," *Appl. Opt.* **33**, 1095–1099 (1994).
14. I. G. Nolt, T. Z. Martin, C. W. Wood, and W. M. Sinton, "Far infrared absorption of the atmosphere above 4.2 km," *J. Atmos. Sci.* **28**, 238–241 (1971).
15. R. E. Hills, A. S. Webster, D. A. Alston, P. L. R. Morse, C. C. Zammit, D. H. Martin, D. P. Rice, and E. I. Robson, "Absolute measurements of atmospheric emission and absorption in the range 100–1000 GHz," *Infrared Phys.* **18**, 819–825 (1978).
16. D. A. Naylor, T. A. Clark, A. A. Schultz, and G. R. Davis, "Atmospheric transmission at submillimetre wavelengths from Mauna Kea," *Mon. Not. R. Astron. Soc.* **251**, 199–202 (1991).
17. E. Serabyn and E. W. Weisstein, "Calibration of planetary brightness temperature spectra at near-millimeter and sub-millimeter wavelengths with a Fourier-transform spectrometer," *Appl. Opt.* **35**, 2752–2763 (1996).
18. E. Serabyn and E. W. Weisstein, "Fourier transform spectroscopy of the Orion molecular cloud core," *Astrophys. J.* **451**, 238–251 (1995).
19. H. J. Liebe, "Atmospheric water vapor: a nemesis for millimeter wave propagation," in *Atmospheric Water Vapor*, A. Deepak, T. D. Wilkerson, and L. H. Ruhnke, eds. (Academic, New York, 1980), pp. 143–201.
20. E. Grossman, *AT User's Manual* (Airhead Software, 2069 Bluff Street, Boulder, Colo. 80302, 1989).
21. M. L. Salby, *Fundamentals of Atmospheric Physics* (Academic, New York, 1996), chap. 8.
22. Eccosorb AN-72, Emerson & Cumming, Inc., Woburn, Mass. 01888.
23. M. L. Kutner and B. L. Ulich, "Recommendations for calibration of millimeter-wavelength spectral line data," *Astrophys. J.* **250**, 341–348 (1981).
24. B. L. Ulich and R. W. Haas, "Absolute calibration of millimeter-wavelength spectral lines," *Astrophys. J. Suppl.* **30**, 247–258 (1976).
25. D. H. Martin, "Polarizing (Martin-Puplett) interferometric spectrometers for the near- and submillimeter spectra," in *Infrared and Millimeter Waves*, K. J. Button, ed. (Academic, New York, 1982), Vol. 6, pp. 65–148.
26. T. J. Sodroski, "Large-scale characteristics of interstellar dust from COBE DIRBE observations" *Astrophys. J.* **428**, 638–646 (1994).
27. M. G. Hauser, "IRAS observations of the diffuse infrared background," *Astrophys. J.* **278**, L15–L18 (1984).
28. J. C. Mather, "Measurement of the cosmic microwave background spectrum by the COBE FIRAS instrument," *Astrophys. J.* **420**, 439–444 (1994).
29. A. Blanco, S. Fonti, M. Mancarella, and A. Piacente, "Reflectivity measurements of Eccosorb," *Infrared Phys.* **25**, 561–562 (1985).
30. R. Goody, *Principles of Atmospheric Physics and Chemistry* (Oxford U. Press, Oxford, 1995), p. 35.
31. M. McKinnon, "Measurement of atmospheric opacity due to water vapor at 225 GHz," Millimeter Array Memo 40 (National Radio Astronomy Observatory, Socorro, N.M., 1987).
32. R. L. Poynter and H. M. Pickett, "Submillimeter, millimeter, and microwave spectral line catalog," *Appl. Opt.* **24**, 2235–2240 (1985); also <http://spec.jpl.nasa.gov/>.
33. E. Serabyn, E. W. Weisstein, and D. C. Lis, "FTS atmospheric transmission measurements and observations of planetary atmospheres," in *The Physics and Chemistry of Interstellar Molecular Clouds*, G. Winnewisser and G. C. Pelz, eds. (Springer-Verlag, Berlin, 1995), pp. 377–379.
34. B. L. Ulich, "Improved correction for millimeter-wavelength atmospheric attenuation," *Astrophys. Lett.* **21**, 21–28 (1980).
35. C. C. Zammit and P. A. R. Ade, "Zenith atmospheric attenuation measurements at millimetre and sub-millimetre wavelengths," *Nature (London)* **293**, 550–552 (1981).